Journal Name

ARTICLE TYPE

Cite this: DOI: 00.0000/xxxxxxxxxx

Polariton Induced Conical Intersection and Berry Phase.†

Marwa H. Farag,*[a] Arkajit Mandal,[a] and Pengfei Huo*[a,b]

Received Date
Accepted Date

DOI: 00.0000/xxxxxxxxxx

We investigate the Polariton induced conical intersection (PICI) created from coupling a diatomic molecule with the quantized photon mode inside an optical cavity, and the corresponding Berry Phase effects. We use the rigorous Pauli-Fierz Hamiltonian to describe the quantum light-matter interactions between a LiF molecule and the cavity, and exact quantum propagation to investigate the polariton quantum dynamics. The molecular rotations relative to the cavity polarization direction play a role as the tuning mode of the PICI, resulting in an effective CI even within a diatomic molecule. To clearly demonstrate the dynamical effects of the Berry phase, we construct two additional models that have the same Born-Oppenheimer surface, but the effects of the geometric phase are removed. We find that when the initial wavefunction is placed in the lower polaritonic surface, the Berry phase causes a π phase-shift in the wavefunction after the encirclement around the CI, indicated from the nuclear probability distribution. On the other hand, when the initial wavefunction is placed in the upper polaritonic surface, the geometric phase significantly influences the couplings between polaritonic states and therefore, the population dynamics between them. These BP effects are further demonstrated through the photo-fragment angular distribution. PICI created from the quantized radiation field has the promise to open up new possibilities to modulate photochemical reactivities.

1 Introduction

Conical intersections (CIs) are ubiquitous in polyatomic molecules and it is known to play an important role in the non-adiabatic dynamics of photochemical reactions.[1–8] At the vicinity of the CI, the energy difference between adiabatic potentials is small and eventually vanishes at the CI, resulting in a large non-adiabatic coupling between the adiabatic states, and a singular non-adiabatic coupling at the CI point. As a result, the the Born-Oppenheimer approximation breaks down[6,9] and the non-adiabatic transitions between electronic states are enhanced.[10–12] CIs are known to play a key role in the relaxation dynamics of most polyatomic molecules and it provides pathways for an ultrafast population transfer between electronic states.[13–21] In addition, CIs introduce a nontrivial geoemtric phase, commonly referred to as the Berry phase,[22] for electronic wavefunctions that causes a sign change of the electron wavefunctions when the nuclei complete a closed path around the CI.[22–27] Both enhanced non-adiabatic transitions and the geometric phase are attributed to as characteristic features of the presence of CIs.[8,25,26,28]

In addition to the intrinsic CIs in polyatomic molecules, CIs can also be created by either standing[29,30] or running[31–33] laser waves in a *diatomic molecule*. This type of CIs are *artificially* created through light-matter interactions, and are commonly referred to as the light-induced conical intersection (LICI).[29,30] For diatomic molecules, the angle between the molecular axis and the polarization axis of the classical laser field gives rise to a rotational motion which constitutes a new degrees of freedom (DOF) that allows forming CIs. In polyatomic molecules, LICIs can be formed even without rotation due to the presence of several vibrational degrees of freedom.[34] In contrast to the field-free CIs where the position of the CI and the strength of the non-adiabatic coupling vectors are inherent properties of a molecule and nontrivial to manipulate, in the LICI, one can easily modify the position of the LICIs and the non-adiabtic coupling strength of the CIs by varying the parameters of light-matter couplings, such as the frequency and the intensity of the classical laser.

LICIs open up new directions in which one can modulate the excited-states dynamics and the inherent physical properties of molecules without modifying the structure of the molecules. Thus, it is vital to reveal the characteristic features of these LICIs. Previous theoretical studies, employing the classical description of light, investigated the nature of the LICI in diatomic molecules[32,33,35–40] and to what extent the geometric phase of the LICI is similar to the natural CIs for polyatomic molecule in a field free space.[31,41–43] It has been demonstrated that LICI

---

[a] *Department of Chemistry, University of Rochester, 120 Trustee Road, Rochester, New York 14627, United states; E-mail: mfarag@ur.rochester.edu.*

[b] *The Institute of Optics, Hajim School of Engineering, University of Rochester, Rochester, New York, 14627; E-mail:pengfei.huo@rochester.edu.*

† Electronic Supplementary Information (ESI) available: Additional results for the time-dependent molecular alignment and the nuclear probability density. See DOI: 00.0000/00000000.

strongly impact the spectroscopic and dynamical properties of molecules, such as the molecular alignment, the photodissociation probability, molecular spectra, and the angular distribution of the dissociation photofragment.

Coupling molecular systems to the quantized radiation mode inside an optical cavity can significantly alter the potential energy landscape[44–47], and can enable new chemical reactivities beyond the existing paradigms of chemistry. The molecular rotations relative to the cavity polarization direction play a role as the tuning mode of the PICI, resulting in an effective CI even within a diatomic molecule. We referred to this as polariton induced conical intersection (PICI).[48,49] The PICI in the diatomic molecules have been theoretically investigated as well.[48–52] These theoretical works reported a significant effect on the spectroscopic and dynamical properties of diatomic molecules in optical cavities. However, to the best of our knowledge, no previous works have studied the geometric phase effect of the PICI created by the cavity quantum radiation field and explained to what extent the Berry phase affects the non-adiabatic dynamics of the molecule-cavity hybrid system.

In the present paper, we use the rigorous Pauli-Fierz Hamiltonian to describe the quantum light-matter interactions between a LiF molecule and the cavity, and exact quantum propagation to investigate the polariton quantum dynamics. To clearly demonstrate the dynamical effects of the Berry phase, we construct two additional models that have the same Born-Oppenheimer surface, but the effects of the geometric phase are removed. We find that when the initial wavefunction is placed in the lower polaritonic surface, the Berry phase causes a π phase-shift in the wavefunction after the encirclement around the CI, indicated from the nuclear probability density and the photo-fragment angular distribution. These BP effects from PICI has the promise to open up new possibilities to modulate photochemical reactivities.

2 Theory

2.1 The Pauli-Fierz Hamiltonian

To investigate the light-induced conical intersection in the framework of cavity quantum electrodynamics (C-QED), we employ a two-level molecular system linearly coupled to a quantized radiation field inside the cavity. The light-matter interaction is described by using the Pauli-Fierz (PF) non-relativistic QED Hamiltonian[53–55], which can be rigorously derived[54,56,57] by applying the Power-Zienau-Woolley (PZW) Gauge transformation[58,59] and a unitary phase transformation[57] on the minimal-coupling Hamiltonian in the Coulomb gauge (*i.e.* the "p · A" Hamiltonian) under the long-wavelength limit. For a molecule coupled to a single photon mode inside an optical cavity, the PF Hamiltonian[60–62] is expressed as

$$\hat{H}_{\mathrm{PF}} = \hat{H}_{\mathrm{M}} + (\hat{a}^{\dagger}\hat{a} + \frac{1}{2})\hbar\omega_{\mathrm{c}} + \sqrt{\frac{\hbar\omega_{\mathrm{c}}}{2}}\,(\hat{a}^{\dagger} + \hat{a})\,\boldsymbol{\lambda}\cdot\hat{\boldsymbol{\mu}} + \frac{1}{2}(\boldsymbol{\lambda}\cdot\hat{\boldsymbol{\mu}})^2 \tag{1}$$

$$= \hat{H}_{\mathrm{M}} + \frac{1}{2}\left[\hat{p}^2 + \omega_{\mathrm{c}}^2\left(\hat{q} + \frac{\boldsymbol{\lambda}\cdot\hat{\boldsymbol{\mu}}}{\omega_{\mathrm{c}}}\right)^2\right], \tag{2}$$

where ω_{c} is the frequency of the cavity photon mode, $\hat{q} = \sqrt{\frac{\hbar}{2\omega_{\mathrm{c}}}}(\hat{a}^{\dagger} + \hat{a})$ and $\hat{p} = i\sqrt{\frac{\hbar\omega_{\mathrm{c}}}{2}}(\hat{a}^{\dagger} - \hat{a})$ represent the displacement coordinate $\hat{q}$ and the conjugate momentum $\hat{p}$ of the quantized photon field.

For the molecular Hamiltonian $\hat{H}_{\mathrm{M}}$, we use a well-parameterized diabatic model of the LiF molecule[63] to investigate the molecule-cavity QED enabled new phenomena. The model contains two diabatic states, the ionic state $|\mathrm{I}\rangle$ and the covalent state $|\mathrm{C}\rangle$, and $\hat{H}_{\mathrm{M}}$ in the $|\mathrm{I}\rangle, |\mathrm{C}\rangle$ electronic subspace is expressed as

$$\hat{H}_{\mathrm{M}} = \left(-\frac{\hbar^2}{2m_0}\nabla_R^2 + \frac{\hat{L}_\theta^2}{2m_0\hat{R}^2}\right)\otimes\hat{\mathbb{1}}_{\mathrm{e}} + \begin{bmatrix}\hat{V}_{\mathrm{I}}(R) & \hat{V}_{\mathrm{IC}}(R)\\ \hat{V}_{\mathrm{CI}}(R) & \hat{V}_{\mathrm{C}}(R)\end{bmatrix} \tag{3}$$

where $\hat{\mathbb{1}}_{\mathrm{e}} = |\mathrm{C}\rangle\langle\mathrm{C}| + |\mathrm{I}\rangle\langle\mathrm{I}|$ is the identity operator in electronic subspace, R is the dissociation coordinate, $\hat{L}_\theta^2 = -\hbar^2\frac{1}{\sin\theta}\frac{\partial}{\partial\theta}\sin\theta\frac{\partial}{\partial\theta}$, is the angular momentum operator[64] of the LiF molecule, and m_0 is the reduced mass of the LiF molecule. Explicitly diagonalizing the matrix of $\hat{V}$ in Eq. 3 provides the adiabatic energy as well as two adiabatic states, $|g(R)\rangle$ and $|e(R)\rangle$, which parametrically depend on nuclear coordinates.

Under the diabatic representation, the dipole operator $\hat{\boldsymbol{\mu}}$ is expressed as

$$\hat{\boldsymbol{\mu}} = \boldsymbol{\mu}_{\mathrm{I}}(R)|\mathrm{I}\rangle\langle\mathrm{I}| + \boldsymbol{\mu}_{\mathrm{C}}(R)|\mathrm{C}\rangle\langle\mathrm{C}|. \tag{4}$$

Note that $\{\mathrm{I},\mathrm{C}\}$ are *eigenstates* of $\hat{\boldsymbol{\mu}}$ in the *truncated electronic subspace*, which are commonly referred to as the Mulliken-Hush diabatic states[63,65–68], and are commonly used as approximate *diabatic* states that are defined based on their characters (covalent and ionic). In this work, we explicitly assume that $|\mathrm{I}\rangle$ and $|\mathrm{C}\rangle$ are strict diabatic states, hence $\langle\mathrm{C}|\nabla_{\mathbf{R}}|\mathrm{I}\rangle = 0$ (they are **R**-independent).

The cavity photon mode and the molecule are coupled through the $\boldsymbol{\lambda}\cdot\hat{\boldsymbol{\mu}}$ term in Eq. 1, where $\boldsymbol{\lambda}$ is expressed as follows

$$\boldsymbol{\lambda} = \sqrt{\frac{1}{\varepsilon_0\mathscr{V}}}\,\hat{\mathbf{e}} \equiv \lambda\hat{\mathbf{e}}, \tag{5}$$

which characterizes the light-matter coupling vector oriented in the direction of polarization unit vector $\hat{\mathbf{e}}$, $\mathscr{V}$ indicates the quantization volume for the photon field, and ε_0 is the permittivity inside the cavity. We denote the angle between the dipole vector $\hat{\boldsymbol{\mu}}$ and $\hat{\mathbf{e}}$ as θ, and $\hat{\mu} = |\hat{\boldsymbol{\mu}}|$, hence the light-matter coupling can be expressed as

$$\boldsymbol{\lambda}\cdot\hat{\boldsymbol{\mu}} = \lambda\hat{\mu}\cos\theta. \tag{6}$$

The Hamiltonian in Eq. (1) can be recast as

$$\hat{H}_{\mathrm{PF}} = \hat{H}_{\mathrm{M}} + (\hat{a}^{\dagger}\hat{a} + \frac{1}{2})\hbar\omega_c + \sqrt{\frac{\hbar\omega_c}{2}}\,(\hat{a}^{\dagger} + \hat{a})\,\lambda\hat{\mu}\cos\theta + \frac{1}{2}(\lambda\mu\cos\theta)^2. \tag{7}$$

The polariton state $|\alpha(\boldsymbol{X})\rangle$ is defined through the following eigen equation

$$\hat{H}_{\mathrm{pl}}|\alpha(\boldsymbol{X})\rangle \equiv (\hat{H}_{\mathrm{PF}} - \hat{T})|\alpha(\boldsymbol{X})\rangle = E_\alpha(\boldsymbol{X})|\alpha(\boldsymbol{X})\rangle, \tag{8}$$

where the polariton Hamiltonian is expressed as $\hat{H}_{\mathrm{pl}} = \hat{H}_{\mathrm{PF}} - \hat{T}$, and the $\hat{T}$ is the vibrational and rotational nuclear kinetic energy of the molecule in Eq. 3. Note that $|\alpha(\boldsymbol{X})\rangle$ is not necessarily a single valued vector. The polariton potential energy surface $E_\alpha(\boldsymbol{X})$ is the eigenvalue of $\hat{H}_{\text{pl}}$ that parametrically dependents on nuclear configuration $\boldsymbol{X}$. This equation is numerically solved by using the diabatic-Fock basis, $\{|\text{I}\rangle\otimes|n\rangle, |\text{C}\rangle\otimes|n\rangle\}$, with the Fock states of the radiation mode (vacuum photon field) $\{|n\rangle\}$, *i.e.*, the eigenstate of $(\hat{a}^\dagger\hat{a}+\frac{1}{2})\hbar\omega_{\text{c}}$.

2.2 Polariton Berry Phase

The Berry phase[22,69], also known as the geometrical phase, is the sign change of the electronic adiabatic wavefunction when the nuclei follow a closed path around the CI. This sign change is canceled out by a corresponding sign change in the boundary condition of the nuclear wavefunction, ensuring that the total wavefunction is single valued. The Berry phase is one of the main characteristic features of the CI and can be seen as a fingerprint for the presence of CIs.[25,43,70,71] Here, we investigate the Berry phase signatures for the PICI created by the quantized radiation field of the cavity.

To simplify our discussion of BP in molecular cavity QED, let us restrict to the subspace of $\{|g(\boldsymbol{X}),1\rangle, |e(\boldsymbol{X}),0\rangle\}$, where the nuclear coordinate is $\boldsymbol{X}\equiv\{R,\theta\}$. The g and the e correspond to the molecular adiabatic electronic states of LiF, while 0 and 1 correspond to the Fock states of the cavity photon mode. This effectively confined the system within the Jaynes-Cummings (JC) model[72] subspace. We emphasize that this is only used for analyzing the BP effect, whereas all of the numerical simulations of the polariton quantum dynamics are performed using the $\hat{H}_{\text{PF}}$ within a large enough basis to converge the results. In this subspace, the two photo-dressed adiabatic states can be viewed as diabatic states, because $\langle g,1|\nabla_{\boldsymbol{X}}|e,0\rangle = \langle g|\nabla_{\boldsymbol{X}}|e\rangle\cdot\langle 1|0\rangle = 0$ due to the orthogonality among vacuum's Fock states. Within the subspace, the polaritonic states can be analytically expressed as follows

$$|+,0(\boldsymbol{X})\rangle = \sin\varphi(\boldsymbol{X})|g,1\rangle + \cos\varphi(\boldsymbol{X})|e,0\rangle, \tag{9}$$

$$|-,0(\boldsymbol{X})\rangle = \cos\varphi(\boldsymbol{X})|g,1\rangle - \sin\varphi(\boldsymbol{X})|e,0\rangle, \tag{10}$$

with the mixing angle

$$\varphi(\boldsymbol{X}) = \frac{1}{2}\arctan\frac{2\langle g,1|\hat{H}_{\text{pl}}|e,0\rangle}{E_{g1}(\mathbf{X})-E_{e0}(\mathbf{X})}, \tag{11}$$

where $\langle g,1|\hat{H}_{\text{pl}}|e,0\rangle = \sqrt{\frac{\hbar\omega_{\text{c}}}{2}}\langle 1|(\hat{a}^\dagger+\hat{a})|0\rangle\cdot\langle g|\boldsymbol{\lambda}\cdot\hat{\boldsymbol{\mu}}|e\rangle$, and the energies are $E_{g1}(\mathbf{X}) = \langle g,1|\hat{H}_{\text{pl}}|g,1\rangle$ and $E_{e0}(\mathbf{X}) = \langle e,0|\hat{H}_{\text{pl}}|e,0\rangle$. When the nuclear coordinates complete a closed path around the CI point, varying $\varphi(\boldsymbol{X})$ from 0 to π causes the polariton adiabatic wavefunctions $|-,0(\boldsymbol{X})\rangle$ and $|+,0(\mathbf{X})\rangle$ alter their sign, causing the accumulation of the geometrical phase. As a result, the electronic wavefunction becomes double valued.

The Berry phase is defined as[9,25,73]

$$\gamma_\alpha(C) = i\oint_C\langle\alpha|\nabla_{\boldsymbol{X}}|\alpha\rangle\, d\boldsymbol{X} = -i\int_S \nabla\times\langle\alpha(\boldsymbol{X})|\nabla_{\boldsymbol{X}}|\alpha(\boldsymbol{X})\rangle\, dS \tag{12}$$

where $|\alpha\rangle$ is the single valued polariton adiabatic wavefunction. Note that by changing line integral to the surface integral during the second equality of Eq. 12, one no longer requires the wavefunction to be a single valued function,[22] because the derivative is directly acting on the Hamiltonian operator instead of the wavefuntion. Hence, all $|\alpha(\boldsymbol{X})\rangle$ from Eq. 8 can be used. On the other hand, one can define the single-valued polariton wavefucntion as[25] $|\alpha\rangle = e^{-i\varphi(\boldsymbol{X})}|\alpha(\boldsymbol{X})\rangle$, and the berry phase becomes

$$\begin{aligned}\gamma_\alpha(C) &= i\oint_C\langle\alpha(\mathbf{X})|e^{i\varphi(\boldsymbol{X})}\nabla_{\boldsymbol{X}}e^{-i\varphi(\boldsymbol{X})}|\alpha(\boldsymbol{X})\rangle d\boldsymbol{X} \qquad (13)\\ &= \oint_C\nabla_{\mathbf{X}}\varphi(\boldsymbol{X})d\boldsymbol{X} + i\oint_C\langle\alpha(\mathbf{X})|\nabla_{\boldsymbol{X}}|\alpha(\boldsymbol{X})\rangle d\boldsymbol{X} = \oint_C\nabla_{\mathbf{X}}\varphi(\boldsymbol{X})d\boldsymbol{X},\end{aligned}$$

where we used the fact that $\langle\alpha(\mathbf{X})|\nabla_{\boldsymbol{X}}|\alpha(\boldsymbol{X})\rangle = 0$ because $|\alpha(\boldsymbol{X})\rangle$ is a pure real basis. This is because that $\nabla_{\boldsymbol{X}}\langle\alpha(\mathbf{X})|\alpha(\boldsymbol{X})\rangle = \nabla_{\boldsymbol{X}}\cdot 1 = 0$ hence $\langle\nabla_{\boldsymbol{X}}\alpha(\mathbf{X})|\alpha(\boldsymbol{X})\rangle + \langle\alpha(\mathbf{X})|\nabla_{\boldsymbol{X}}\alpha(\boldsymbol{X})\rangle = 0$. Also note that $\langle\nabla_{\boldsymbol{X}}\alpha(\mathbf{X})|\alpha(\boldsymbol{X})\rangle = \langle\alpha(\mathbf{X})|\nabla_{\boldsymbol{X}}\alpha(\boldsymbol{X})\rangle^*$, hence leading to the results that $\langle\alpha(\mathbf{X})|\nabla_{\boldsymbol{X}}|\alpha(\boldsymbol{X})\rangle = 0$ if it is pure real.

With Eq. 13, one can numerically evaluate the Berry phase by line integral of $\nabla_{\mathbf{X}}\varphi(\boldsymbol{X})d\boldsymbol{X}$. Choosing a particular path of encriclement that centered at (R_0,θ_0), with a radius ρ and encirclement angle ϕ depicted in Fig. 1c, such that

$$R = R_0 - \rho\cos\phi;\quad \theta = \theta_0 + \rho\sin\phi. \tag{14}$$

The Berry phase along this encircled path is[25]

$$\gamma_\alpha(C;\boldsymbol{X}) = \oint_C\nabla_{\mathbf{X}}\varphi(\boldsymbol{X})d\boldsymbol{X} = \oint_C d\varphi(\boldsymbol{X}) = \varphi(\phi)|_0^{2\pi} = \pi, \tag{15}$$

suggesting that there is an additional π phase shift and can be calculated from the difference of the diabatic-adiabatic transformation angle $\varphi(\boldsymbol{X})$ (see Eq. 11) at the beginning and at the end of the closed path.[25,31]

Figure 1a presents the schematic illustration of the LiF molecule couple to the cavity, with θ as the angle between the polarization direction of the cavity photon mode and the direction of the molecular dipole moment.

Figure 1b presents the polariton potential energy surface (PES) $E_\alpha(\boldsymbol{X})$ obtained from diagonalizing the matrix of $\hat{H}_{\text{pl}}$ in Eq. 8, with ten Fock state employed to achieve convergence. As one can see, the polaritonic surfaces give rise to a conical intersection (CI) at $R\approx 5$ a.u. and $\cos\,\theta = 0\,(\theta = \pi/2)$. This type of conical intersection is referred to as the Polariton Induced Conical Intersection (PICI), arising due to the rotational DOF of the diatomic molecule coupled to the radiation field.

Figure 1c presents three different enclosing path in the nuclear configuration space $\boldsymbol{X} = \{R,\theta\}$, where only one path (red) is looped around the PICI. Figure 1d presents the value of the mixing angle $\varphi(\phi)$ (Eq. 11) at a particular value of the encirclement angle ϕ along the path presented in Figure 1c with the same color-coding. The Berry phase along a path is expressed as $\gamma_\alpha(C;R,\theta) = \int_0^{2\pi}\nabla_{\mathbf{X}}\varphi(\boldsymbol{X})d\boldsymbol{X} = \varphi(2\pi)-\varphi(0)$, as a function of the encirclement angle ϕ. As shown in Figure 1d, following a full circle around the PICI (red), the initial and final $\varphi(R,\theta)$ is changed by π. On the other hand, when the path does not encircle around the PICI, the difference between the initial and final $\varphi(R,\theta)$ is zero. In the former case, the polariton wavefunctions are double valued, while in the latter case, the polariton wavefunctions are single valued.

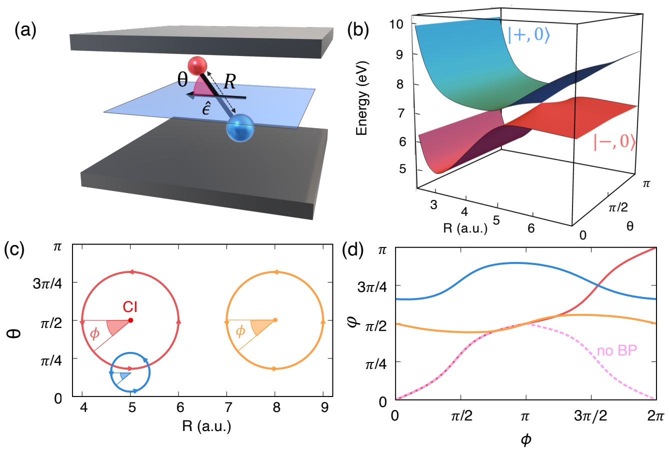

Fig. 1 (a) The angle between the polarization direction of the cavity photon mode and the direction of the molecular dipole moment. (b) The polaritonic potential energy surface ($|-,0\rangle$ and $|+,0\rangle$) as a function of the dissociation coordinate (R) and the angular coordinate (θ) for a cavity coupling $\lambda = 0.04\sqrt{2/\hbar\omega_c}$. (c) The contours used in the Berry phase calculations. (d) The transformation angle φ (Eq. 11) as a function of the encirclement angle ϕ.

Further analysis is performed by artificially removing the Berry phase using the approach described in Ref. 74. This approach eliminate the berry phase from the diabatic Hamiltonian by using the absolute value of the coupling $|\langle g,1|\hat{H}_{\rm pl}|e,0\rangle|$ instead of its original expression $\langle g,1|\hat{H}_{\rm pl}|e,0\rangle$ inside the mixing angle φ (see Eq. 11). Using this approach, one can remove the presence of the Berry phase with the same encirclement path (red circle in Fig. 1c), giving rise to the phase change indicated with the magenta curve in Fig. 1d. As one can notice, when the Berry phase is removed the difference between the initial and final $\gamma(R,\theta)$ is zero. Consequently, the corresponding polariton wavefunctions in Eqs. 9-10 remain single-valued. Therefore, the CI created by the quantized cavity filed gives rise to a Berry phase with a π phase shift, similar to the Berry phase of the CI in molecules[25] and the CI created by the classical laser field in the Floquet picture.[31,74,75]

2.3 Computational Details

To solve the time-dependent Schrödinger equation of the molecule-cavity hybrid system, the dynamics is propagated with the numerically exact method based on the discrete variable representation (DVR) approach.[9,64] The angular coordinate is represented by the Legendre polynomial[64] $P_j^m(\cos\theta)$ with $m = 0$ and $j = 0, 1, \ldots, N_\theta - 1$, where the number of the basis function N_θ equals 101. The dissociation coordinate of LiF, on the other hand, is represented by the sin-DVR[64] with number of basis function N_R equals 1170 for the range of $1.8 \le R \le 60$ (a.u.). The electronic and photonic DOFs are represented by using the diabatic-Fock basis, $\{|\mathrm{I}\rangle \otimes |n\rangle, |\mathrm{C}\rangle \otimes |n\rangle\}$, with $|n\rangle$ as the Fock states of the radiation mode. The equation of motions are solved using the fourth-order Runge-Kutta integrator and the time step $\Delta t = 0.005$ fs. All the simulations are carried out by employing the Pauli-Fierz Hamiltonian.

The initial wavefunctions are prepared as the product of the ground vibrational state $|v\rangle$ of the LiF located around $R \approx 3$ a.u. on the $|\mathrm{I}\rangle$ electronic state (ground electronic states), with either $J = 0$ or $J = 1$ quantum number for the rotational DOF. The wavefunction with $J = 0$ is symmetric, while the wavefunction with $j = 1$ is asymmetric with respect to $\theta = \pi/2$ (see Figure 3 a,c). The initial wavefunction is then placed either in the $|\mathrm{I},1\rangle$ state or the $|\mathrm{C},0\rangle$ surface for the subsequent propagation. When the wavepacket is placed in the $|\mathrm{I},1\rangle$ surface, we apply a shift of the wavefunction along the dissociation coordinate by 0.8 a.u. The wavefunction is centered at $R \approx 2.2$ a.u. instead of 3.0 a.u. along the dissociation coordinate. This value is chosen to overcome an initial barrier in the $|\mathrm{I},1\rangle$ surface to facilitate the dynamical evolution of the hybrid system.

To analyze the effect of the Berry phase on the calculated quantities, we compare the results obtained from the 2D model with two other models where the effect of the CI is theoretically eliminated. The first model is referred to as the one-dimensional (1D) model,[32] in which the angular momentum operator is set to be zero ($\hat{L}_\theta = 0$ in Eq. 3). As a consequence, there is no dynamical evolution along the angular coordinate and θ is treated as a parameter in the potential. The second model is referred to as the non-BP model, where the Berry phase is artificially removed by replacing $\hat{\boldsymbol{\lambda}} \cdot \hat{\boldsymbol{\mu}}$ by its absolute value.[74] As a consequence, the originally double-valued polariton wavefunction is forced to be single-valued.[74]

3 Results and Discussion

Fig. 2 presents the potential energy surface (PES) of the LiF model system, as well as the polariton quantum dynamics *without* considering the rotational DOF (by setting $\hat{L}_\theta^2 = 0$ in Eq. 3). Fig. 2a presents the diabatic potentials energy surface $V_\alpha(R)$ of the $|\mathrm{I}\rangle$ state (red) and $|\mathrm{C}\rangle$ state (blue) in a LiF molecule, respectively. The crossing of these two *diabatic* curves occur at $R = R_0 \approx 13.5$ a.u., forming an avoided crossing between the adiabatic states $|g\rangle$ and $|e\rangle$ (not shown here). The diabatic coupling is $V_{\mathrm{IC}}(R)$ (gold line). Fig. 2e-f presents the exact polariton quantum dynamics of the model system (e) with dipole self energy (solid lines) and (f) without dipole self energy (DSE) term. The DSE is the last term in Eq. 1 in the PF Hamiltonian. Ignoring DSE gives incorrect polariton surfaces and also incorrect polariton quantum dynamics, hence, leading to incorrect polariton quantum dynamics, such as missing the $|G,0\rangle$ population.

Fig. 2b presents the matrix elements of $\hat{\boldsymbol{\mu}}$ in both the diabatic (solid lines) and the adiabatic (dashed lines) representations. The ionic permanent dipole (solid red) $\boldsymbol{\mu}_{\mathrm{I}}(R)$ increases linearly with R, while the covalent permanent dipole (solid blue) $\boldsymbol{\mu}_{\mathrm{C}}(R) \approx 0$, as one expects. The adiabatic states switch their characters around R_0, as a result, the adiabatic permanent dipole switches in that region, and $\mu_{eg}(R)$ peaks at R_0 as the two diabatic states couple strongly around R_0. Fig. 2c-d presents the polariton potential energy surface $E_\alpha(R)$ defined in Eq. 8, (c) with the dipole self-energy (DSE) $\frac{1}{2}(\hat{\boldsymbol{\lambda}} \cdot \hat{\boldsymbol{\mu}})^2$ term (see Eq. 1) and (d) without considering DSE. Note that even though we label these polariton states with a "photon number" (such as $|\pm,0\rangle$), they are the eigenstate of $\hat{H}_{\rm pl}$. Here, a strong light-matter coupling ($\lambda = 0.04\sqrt{2/\hbar\omega_c}$) is used and the frequency of the cavity photon mode is 3.995 eV. Un-

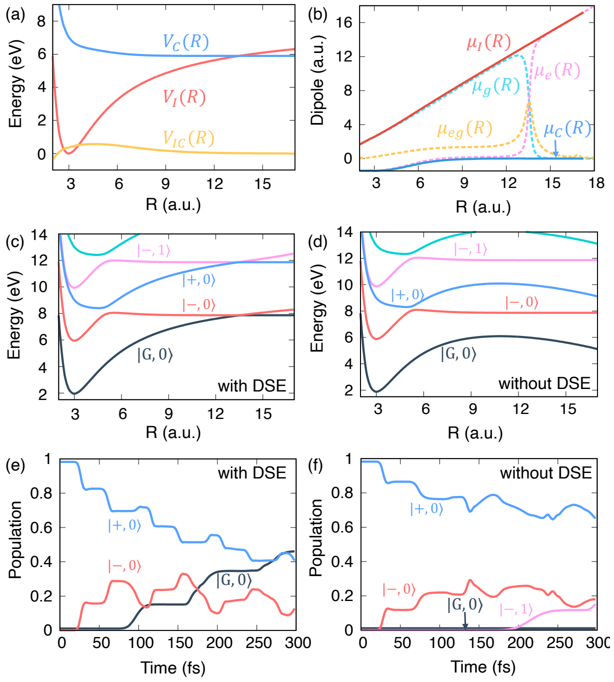

Fig. 2 (a) The diabatic potential energy surface of the LiF as a function of the dissociataion coordinate (R). (b) The LiF permanent and transition dipole moment in the diabatic and adiabatic representation. (c) The polaritonic potential energy surface with dipole self energy (DSE) term and (d) without DSE term for a cavity coupling $\lambda = 0.02\sqrt{2/\hbar\omega_c}$. (e) The time evolution of the polaritonic state population with DSE term and (f) without DSE term.

like a previous work on LiF couple to the quantized cavity field[49], we explicitly account for the dipole self-energy to compute the full Hamiltonian for the LiF in an optical cavity. We find that under a moderate and a strong light-matter coupling λ, excluding the DSE results in an incorrect potential energy surface. As we can clearly see, without the DSE, the ground state is no-longer bonded and becomes dissociative at a large nuclear distance.[60,76,77]

Fig. 3 presents the nuclear probability density (NPD) of the $|-,0\rangle$ state before and after the encirclement around the PICI with the full 2D model that explicitly consider the rotational DOF. The initial rotational wavefunction is chosen as (a)-(b) $J = 0$ and (c)-(d) $J = 1$. The initial excitation places the wavepacket on the lower polariton surface $|-,0\rangle$, and the polariton dynamical evolve predominately on the same surface (through adiabatic dynamical evolution). One notices that both $J = 0$ and $J = 1$ rovibrational wavefunctions alter their symmetries with respect to $\theta = \pi/2$ after encircling around the CI. For $J = 0$ (Fig. 3a-b), the initial polariton wavefunction is symmetric with respect to $\theta = \pi/2$ before the encirclement (Fig. 3a), and it becomes asymmetric after passing around the CI (Fig. 3b). This is caused by a destructive interference at $\theta = \pi/2$ due to the BF accumulation for the clock-wise and counter clock-wise path, manifesting into a node in the NPD. On the contrary, in the $J = 1$ case (Fig. 3c-d), the initial wavefunction is asymmetric with respect to $\theta = \pi/2$ (Fig. 3c), and it becomes symmetric after encircling around the CI (Fig. 3d). This is caused by a constructive interference at $\theta = \pi/2$.

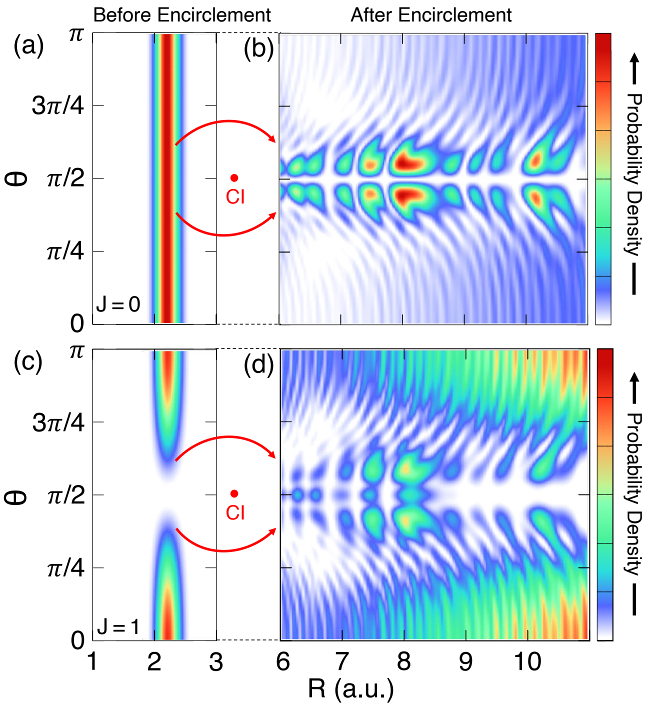

Fig. 3 The nuclear probability density obtained from the 2D model with the initial excitation to the the lower polariton state $|-,0\rangle$. Left: before the encirclement ($t = 0$ fs) and right: after the encirclement ($t = 134$ fs) for the initial rotational quantum number $J = 0$ (a,b) and $J = 1$ (c,d).

Fig. 4 presents the NPD by theoretical eliminating the effects of BP, using either the non-BP model in panel (a) and (c) or the 1D model in panel (b) and (d). The former neglect the effect of the Berry phase, whereas the latter prevents the dynamics along the angular coordinate. To illustrate how the character of the Berry phase is manifested in the wavefunction dynamics, we compare the NPD obtained from these two models with the NPD obtained with the full 2D model in Fig. 3. Unlike the 2D model, the symmetry of the initial wavefunction in the non-BP model do not change after passing around the CI. In particular, the rovibrational wavefunction with $j = 0$ remains symmetric after it passing the CI (Fig. 4a) and the rovibrational wavefunction $J = 1$ stays asymmetric with respect to $\theta = \pi/2$ after encircling around the CI (Fig. 4c). Similarly, in the 1D model (Fig. 4b and d),we notice both rovibrational wavefunction with (b) $J = 0$ and (d) $J = 1$ have a zero amplitude at $\theta = \pi/2$. In the 1D model, the angular momentum operator is set to be zero, hence the dynamics along the angular coordinate θ is not permitted. As a result, the rovibrational wavefunction does not encircle around the CI. This explains the absent of amplitudes at $\theta = \pi/2$ for both $J = 0$ and $J = 1$ cases in the 1D model, due to the fact that the angler DOF is treated as a static parameter in the model. These results further corroborate that the NPD pattern observed in the 2D model in Fig. 3 is a direct signature of the Berry phase due to the encirclement of the wavefunction around the PICI.

To further interpret different interference patterns of the wavefunction after the encirclement around the CI in the 2D model and the non-BP model, we adapt the Feynman path unwind-

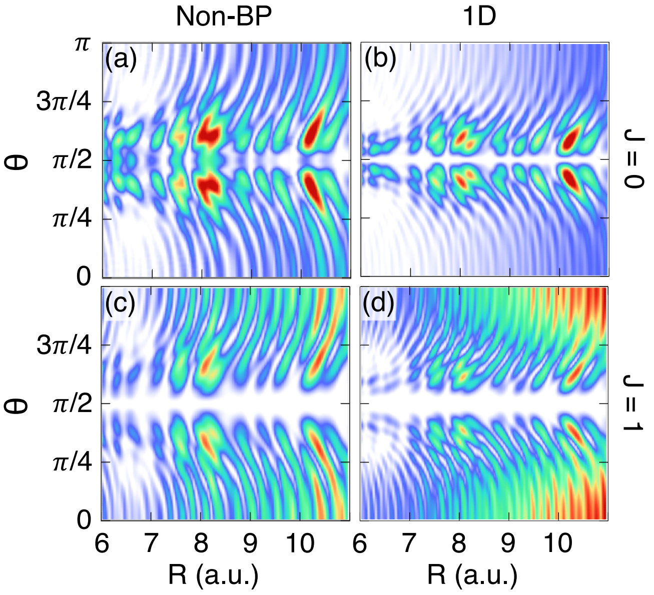

Fig. 4 The nuclear probability density of the $|-,0\rangle$ state obtained from the non-BP and 1D models at $t = 134$ for the rovibrational wavefunction $J = 0$ (a,b) and $J = 1$ (c,d).

ing approach of Althorpe and co-workers[27,78] which can be directly applied to the system confined to the lower adiabatic surface. Due to the presence of CI, there are inaccessible region in the space, resulting in *multiply connected space* in the language of topology. As a consequence, the paths around the CI can be classified according to the number of loops around the CI.[78] All Feynman Paths can be group into two distinct classes, one corresponds to all even number of loops and another with all odd number of loops. The even loops (e) correspond to the Feynman paths encircling clockwise around the CI, whereas the odd loops (o) correspond to the Feynman paths encircling counterclockwise around the CI.[27] Althorpe and co-workers demonstrate that the effect of the geometric phase is to change the relative sign between the even (e) and odd (o) loops on the time evolution operator as $K(\boldsymbol{X},\boldsymbol{X}_0|t) = K_{\mathrm{e}}(\boldsymbol{X},\boldsymbol{X}_0|t) - K_{\mathrm{o}}(\boldsymbol{X},\boldsymbol{X}_0|t)$, whereas without considering the geometric phase, the propagator is $\tilde{K}(\boldsymbol{X},\boldsymbol{X}_0|t) = K_{\mathrm{e}}(\boldsymbol{X},\boldsymbol{X}_0|t) + K_{\mathrm{o}}(\boldsymbol{X},\boldsymbol{X}_0|t)$, $\boldsymbol{X}_0$ denotes the initial nuclear configuration and $\boldsymbol{X}$ refers to the nuclear configuration at time t. The kernel operator propagates the initial wavefunction $\Psi(\boldsymbol{X}_0,0)$ and gives[27,78] $\Psi_{\mathrm{e}}(\boldsymbol{X},t) = \int d\boldsymbol{X}_0\, K_{\mathrm{e}}(\boldsymbol{X},\boldsymbol{X}_0|t)\, \Psi(\boldsymbol{X}_0,0)$ and $\Psi_{\mathrm{o}}(\boldsymbol{X},t) = \int d\boldsymbol{X}_0\, K_{\mathrm{o}}(\boldsymbol{X},\boldsymbol{X}_0|t)\, \Psi(\boldsymbol{X}_0,0)$. The final wavefunction after the encirclement can therefore be expressed as

$$\Psi(\boldsymbol{X},t) = \frac{1}{\sqrt{2}}\left[\Psi_{\mathrm{e}}(\boldsymbol{X},t) - \Psi_{\mathrm{o}}(\boldsymbol{X},t)\right] \tag{16}$$

$$\tilde{\Psi}(\boldsymbol{X},t) = \frac{1}{\sqrt{2}}\left[\Psi_{\mathrm{e}}(\boldsymbol{X},t) + \Psi_{\mathrm{o}}(\boldsymbol{X},t)\right] \tag{17}$$

where $\Psi(\boldsymbol{X},t)$ and $\tilde{\Psi}(\boldsymbol{X},t)$ are the wavefunctions obtained with geometric phase and without geometric phase, respectively. Eqs. (16) and (17) indicate that explicitly consider the geometric phase alters the interference patterns. These patterns of the wavefunctions obtained from the Feynman path theory are consistent with the NPD obtained from the 2D and non-BP models in Fig. 3 and Fig. 4, confirming that the difference between the NPD obtained from the 2D model and the non-BP model is a consequence of the Berry phase.

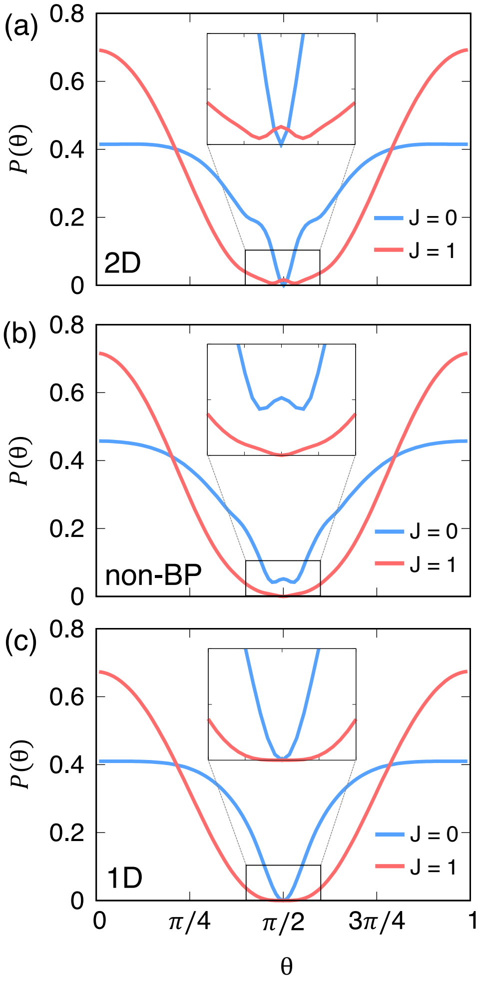

Fig. 5 The normalized photofragment angular distribution obtained from (a) 2D model, (b) non-BP model, and (c) 1D model for the rovibrational wavefunction $j = 0$ and $j = 1$.

We further compute the photofragment angular distribution (PAD) for the two rovibrational wavefunctions $J = 0$ and $J = 1$ from 2D, non-BP, and 1D models. The PAD is defined as[32]

$$P(\theta) = \int_0^{\infty} \langle \Psi_{g0}(t)|\Theta(R - R_D)|\Psi_{g0}(t)\rangle\, dt, \tag{18}$$

where Θ is the Heaviside step function, and $R_D = 19.0$ a.u. is the starting point of the dissociation, $|\Psi_{g0}(t)\rangle = \langle g,0|\Psi(t)\rangle$ is the time-dependent polariton wavefunction projected on the $|g,0\rangle$ surface. The PAD provides details about the direction in which the photodissociation occurs. Figure 5 summarizes the results of the PAD obtained from 2D, non-BP, and 1D models for $J = 0$ and $J = 1$.

Fig. 5 presents the angle-resolved photo-dissociation probability of the LiF occurs, where $\theta = 0$ or $\theta = \pi$ represent directions nearly parallel to the polarization axis of the cavity, and $\theta = \pi/2$ represents a direction perpendicular to the polarization axis of the cavity. The behavior of the PAD at the perpendicular orientation $\theta = \pi/2$ is different for each model. More specifically, in the 2D model (Fig. 5a), we observe a local minimum at $\theta = \pi/2$ for $J = 0$ (blue), and a local maximum for $J = 1$ (red). These results are in contrast to those obtained from the non-BP model (Fig. 5b) in which the Berry phase is absent. In the non-BP model, we observe a local maximum for $J = 0$ (blue) and a local minimum (red) for $J = 1$ at $\theta = \pi/2$. Importantly, we find that there is a π phase-shift at $\theta = \pi/2$ between the PAD obtained from the 2D model and non-BP models. This pattern at $\theta = \pi/2$ is a consequence of the Berry phase. On the other hand, in the 1D model (Fig. 5c), both rovibrational wavefunctions with $J = 0$ and $J = 1$ exhibit a local minimum at $\theta = \pi/2$. This is because the dynamics along the angular coordinate is not permitted in the 1D model. Notably, the PAD obtained from the 2D, non-BP, and 1D models are consistent with the results of NPD presented in Fig. 3-Fig. 4. The results obtained above suggest that by comparing the PAD for $J = 0$ and $J = 1$ molecular species in directions nearly perpendicular to the polarization axis of the cavity photon mode, one can probe the Berry phase of the PICI in diatomic molecules. This findings are reminiscent of a previous work investigating H_2^+ molecule[79] or D_2^+ molecule coupled to an intense classical laser field.[42]

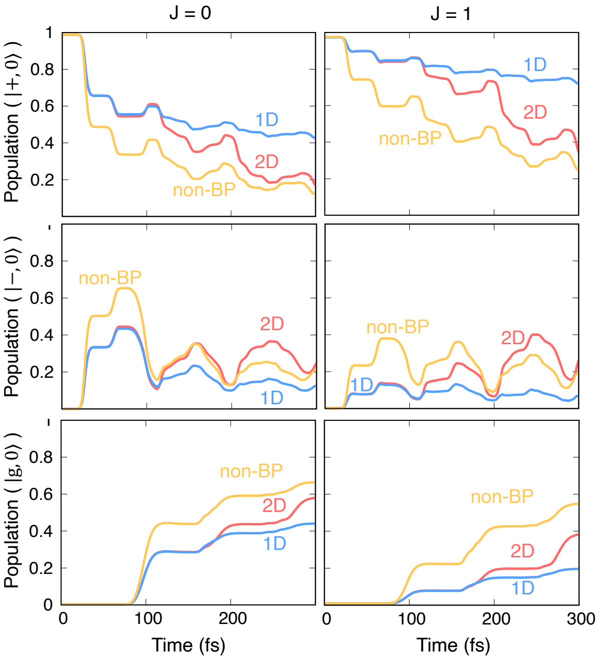

Fig. 6 Population of the polaritonic states for the rovibrational wavefunction $J = 0$ (left panel) and $J = 1$ (right panel).

So far, we have discussed the wavefunction dynamics in the lower polaritonic surface $|-,0\rangle$ and how the Berry phase manifest into the polariton quantum dynamics. We further investigate the polariton dynamics with an initial excitation onto the upper polariton surface $|+,0\rangle$. Unlike the dynamics in the lower polaritonic surface where the region surrounding the CI is inaccessible, when initially excited to the upper polaritonic surface, this region of space is now *accessible* due to the funnel-like shape of the CI. Moreover, the polariton states near the CI become nearly degenerated, causing a significant population transfer between the the upper $|+,0\rangle$ and the lower $|-,0\rangle$ polariton state. From Fig. 1b, one can predict that after a vertical excitation to the upper polaritonic surface $|+,0\rangle$, the initial wavefunction evolves from the Franck-Condon point toward the CI. During this time-evolution, the wavepacket splits into several parts. One part of the wavepacket passes through the CI to the lower polaritonic surface $|-,0\rangle$. The other part of the wavepacket circles around the CI and remains in the upper polaritonic surface, oscillating back and forth between the initial and final nuclear configurations on the upper polaritonic surface. During these oscillations, the wavepacket gradually passes through the CI to the lower polaritonic surface. Note that part of the wavefunction that moves to the lower polaritonic surface is located to the left of the CI. This part of the wavefunction in the lower polaritonic surface adds more complexity to the wavefunction. This is because in addition to the ability of the wavefunction to encircle around the CI in the lower surface, it has enough energy to access point along the CI and passes to the upper polaritonic surface. Because of the complexity of the dynamics with an initial excitation on the upper polaritonic surface, it is difficult to investigate the symmetry of the wavefunction to analyze the Berry phase effect as explained for the lower polaritonic surface. Alternatively, we analyze the effect of the Berry phase using the time-dependent quantities.[80] Fig. 6 presents the population dynamics of the upper $|+,0\rangle$ and the lower $|-,0\rangle$ polariton states as well as the ground state $|g,0\rangle$ of the molecule-cavity hybrid system, obtained from the 2D model (red), the non-BP model (gold), and 1D model (blue), with the initial rotational quantum number $J = 0$ (left) and $J = 1$ (right). In general, we observe that the results with the $J = 0$ and $J = 1$ are qualitatively similar. By comparing the polariton populations obtained from the 2D model and the 1D model, we find that the dynamics for both models are similar at an early time and then deviating at a later time. This is not surprising because the 2D model system does not significantly rotate during this early time dynamical evolution (see Figure S1 in the ESI which presents the degree of the alignment of the LiF as a function of time). After this early time scale (≈ 25 fs), the rotation of the molecule plays a significant role and the two models predicts different results. In the 1D model, the polariton wavefunction was not propagated along the angular coordinate θ to reach the CI region (where the magnitude of the population transfer is the largest due to nearly degenerated polariton energy gap), and therefore, the population transfer from the upper to the lower polaritonic surface is not as significant as the 2D model. This explains why the population transfer magnitude from the upper polaritonic state in the 1D model is smaller than that in the 2D model.

On the other hand, by comparing the non-BP model with the 2D model, we find that the population transfer from the upper polaritonic state is faster in the non-BP model than that in the 2D model. A possible explanation for these results can be rationalize from the diabatic picture and the symmetry along the angular coordinate θ (the coupling coordinate)[42,74] as follows. In the

2D model, the two surfaces $|e,0\rangle$ and $|g,1\rangle$ are coupled through an odd function $\boldsymbol{\lambda}\cdot\hat{\boldsymbol{\mu}} = \lambda\hat{\mu}\cos\theta$ along the angular coordinate θ (where the sign change occurs at $\theta = \pi/2$). In the non-BP model, the two surfaces are coupled by an even function $|\boldsymbol{\lambda}\cdot\hat{\boldsymbol{\mu}}|$ along the angular coordinate. This leads to a difference in the coupling matrix elements between the $|e,0\rangle$ state and the $|g,1\rangle$ states with a particular rotational quantum number.

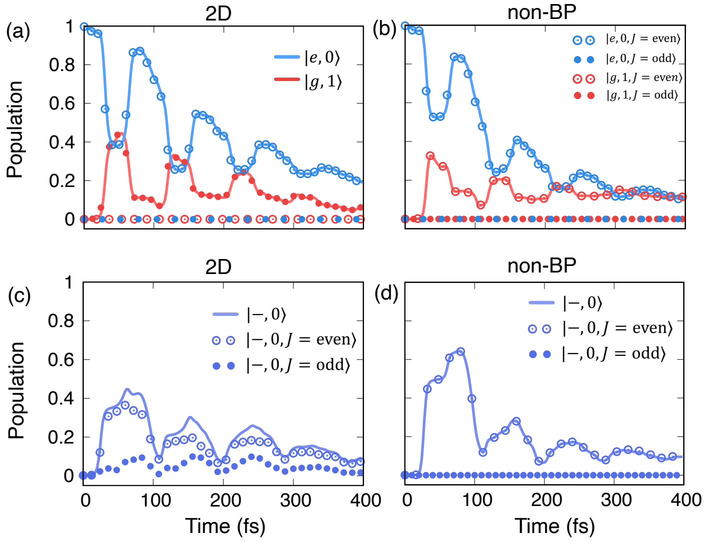

Fig. 7 The contribution of the even and odd rotational quantum number in the population of the $|e,0\rangle$ and $|g,1\rangle$ obtained from the 2D (a) and non-BP (b) models for the $J=0$ initial rovibrational wavefunction. Solid lines introduce the total population in $|e,0\rangle$ and $|g,1\rangle$ and dotted-lines represent the contribution from the even and odd rotational quantum number. The contribution of the even and odd rotational quantum number in the population of the polaritonic state $|-,0\rangle$ in the 2D (c) and non-BP (d) models.

Fig. 7 presents the total population of the $|e,0\rangle$ and $|g,1\rangle$ states obtained from the 2D model (Fig. 7a) and non-BP (Fig. 7b) model as well as the contributions from both the even and odd states of the angular coordinate (Fig. 7c-d). We find that in the 2D model (Fig. 7a) and the initial rotational state $J=0$, the even rotational level in the $|e,0\rangle$ state is coupled with the odd rotational level in the $|g,1\rangle$ surface. As a consequence, only those rotational states with an odd J in $|g,1\rangle$ are populated, while the rotational states with an even J are unimportant. On the other hand, in the non-BP model (Fig. 7 b, the rotational state with an even J in the $|e,0\rangle$ surface is coupled with other even states in the $|g,1\rangle$ surface. As a result, only the even states in $|g,1\rangle$ are populated while the odd states remains un-populated. The quantum dynamics results in Figure 7a-b agree well with these interpretation, showing that in the 2D model (Fig. 7a), only the even-J rotational states are populated in the $|e,0\rangle$ state (blue) and only the odd-J rotational states (filled circles) are populated in the $|g,1\rangle$ state (red), whereas in the non-BP model (Fig. 7b) only the even-J rotational states (open circles) are populated on both $|e,0\rangle$ and $|g,1\rangle$ state. The lower polariton state $|-,0\rangle$ (Fig. 7c-d), which are the superposition states of $|g,1\rangle$ and $|e,0\rangle$, effectively averaging over the transition of many rotational states, resulting in difference between the population transfer from the upper polaritonic state in the 2D and non-BP model.

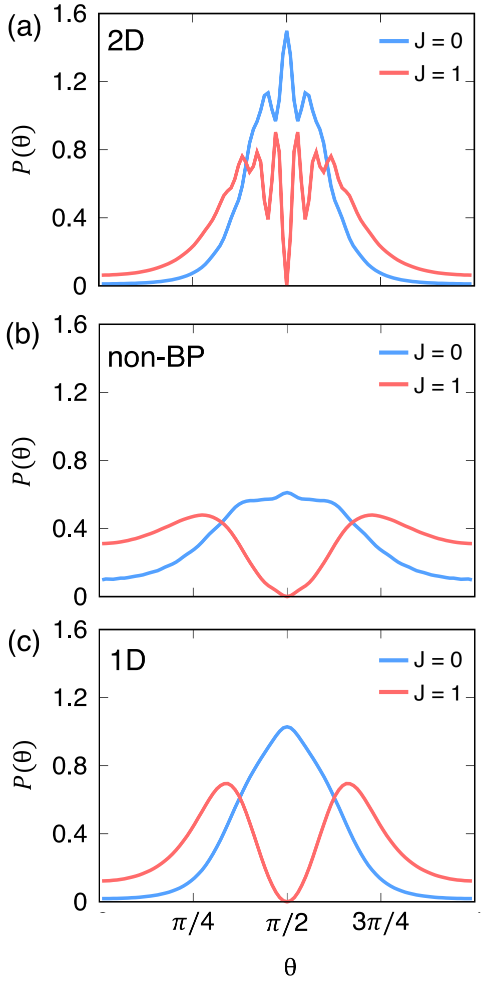

Fig. 8 The normalized photofragment angular distribution for the rovibrational wavefunction $J=0$ and $J=1$.(a) 2D model. (b) non-BP model. (c) 1D model.

Fig. 8 presents the PAD (Eq. 18) obtained from the 2D model (Fig. 8a), the non-BP model (Fig. 8b), and the 1D model (Fig. 8c) with the initial rotational quantum number of $J=0$ (blue) and $J=1$ (red). The results in the 2D model (Fig. 8a) show strong oscillations for both $J=0$ and $J=1$ and are absent in the non-BP (Fig. 8b) and the 1D model (Fig. 8c). When comparing the NPD obtained from the three models before passing through the CI, we find that these oscillations arise in the 2D model after passing the CI. In addition, these patterns do not change during the transition from $|-,0\rangle$ surface to $|g,0\rangle$ surface. The NPD for the the $|-,0\rangle$ and $|g,0\rangle$ states obtained from the 2D, non-BP, and 1D models for rotation quantum number $J=0$ and $J=1$ are shown in Figure S2 in the ESI.

To clearly understand the origin of these oscillations in the PAD from the 2D model, we analyze the contribution of the even and the odd quantum number of the angular coordinate in the total population of the $|-,0\rangle$ state and the results are presented in Figure 7c-d. Figure 7c demonstrates that in the 2D model, the population of the $|-,0\rangle$ has contributions from both even and odd quantum state. This is expected to give rise to both a destructive and a constructive interference between the odd and even rotational wavefunctions, resulting in a strong oscillation in the PAD in the 2D model. On the other hand, Fig 7d demonstrates that the population of the $|-,0\rangle$ in the non-BP model only has contribution from the even-J rotational state. Thus, the interference happens only between even-J rotational wavefunctions with the same symmetry. This explains why the oscillations are absent in the non-BP model. Our results, therefore, demonstrate that the strong oscillation obtained from the 2D model in the PAD are a consequence of the symmetry of the light-matter coupling Hamiltonian $\boldsymbol{\lambda} \cdot \hat{\boldsymbol{\mu}} = \lambda \hat{\mu} \cos\theta$, which also give rise to the BP phase effects.

4 Conclusions

We investigate the impact of the Berry phase introduced by the polariton induced conical intersection (PICIs) by coupling a diatomic molecule (LiF) with the quantized radiation field inside an optical cavity. The Pauli-Fierz Hamiltonian is employed to describe the quantized light-matter interactions. We compare the results obtained from the Pauli-Fierz Hamiltonian with other artificial models where the Berry phase is removed or the wavefunction is not allowed to encircle around the PICI. We find that when the initial wavefunction is placed in the lower polaritonic surface, the Berry phase causes a sign change in the polariton wavefunction symmetry along the angular coordinate, resulting in a change of the interference after encircling the PICI. Our results reveal that the Berry phase causes a π phase shift, akin to those obtained from the naturally existing CI in molecules. In addition, we analyze the Berry phase after excitation to the upper polaritonic surface. Our results reveal that the Berry phase strongly influences the coupling between polaritonic states and therefore, the population transfer between them. Further, we find that the symmetry of the light-matter coupling term is the main source for the observed oscillations in the photo-fragment angular distribution for LiF. The PICI created from the quantized radiation field exhibits a non-trivial geometric phase, opening up new possible direction to manipulate photochemical reactivities of molecules with optical cavities.

Conflicts of interest

There are no conflicts to declare.

Acknowledgements

This work was supported by the National Science Foundation "Enabling Quantum Leap in Chemistry" program under the Grant number CHE-1836546, as well as by a Cottrell Scholar award (a program by Research Corporation for Science Advancement). Computing resources were provided by the Center for Integrated Research Computing (CIRC) at the University of Rochester.

Notes and references

1 E. Teller, *J. Phys. Chem.*, 1937, **41**, 109–116.
2 H. Kuppel and W. Domcke, *Adv. Chem. Phys.*, 1984, **57**, 59–246.
3 A. Dreuw, G. A. Worth, L. S. Cederbaum and M. Head-Gordon, *J. Phys. Chem. B*, 2014, **108**, 19049–19055.
4 S. Matsika and P. Krause, *Annu. Rev. Phys. Chem.*, 2011, **62**, 621–643.
5 W. Domcke, D. R. Yarkony and H. Köppel, *Conical intersection: electronic structures, dynamics and spectroscopy*, World Scientific Publishing Co. Pte. Ltd, 2004.
6 G. A. Worth and L. S. Cederbaum, *Annu. Rev. Phys. Chem.*, 2004, **55**, 127–158.
7 M. H. Farag, T. L. C. Jansen and J. Knoester, *J. Phys. Chem. Lett.*, 2016, **7**, 3328–3334.
8 M. Kowalewski, B. P. Fingerhut, K. E. Dorfman, K. Bennett and S. Mukamel, *Chem. Rev.*, 2017, **117**, 12165–12226.
9 D. J. Tannor, *Introduction to quantum mechanics: A time-dependent perspective*, University Science Books, California, 2007.
10 J. E. Subotnik, E. C. Alguire, Q. Ou, R. B. Landry and S. Fatehi, *Acc. Chem. Res.*, 2015, **48**, 1345–1350.
11 B. G. Levine and T. J. Martinez, *Annu. Rev. Phys. Chem.*, 2007, **58**, 613–634.
12 D. R. Yarkony, *Chem. Rev.*, 2012, **112**, 481–498.
13 J. J. Serrano-Pérez, F. de Vleeschouwer, F. de Proft, D. Mendive-Tapia and M. J. Robb, *J. Org. Chem.*, 2013, **78**, 1874–1886.
14 B. Joalland, T. Mori and T. J. Martinez, *J. Phys. Chem. Lett.*, 2014, **5**, 1467–1471.
15 R. W. Schoenlein, L. A. Peteanu, R. A. Mathies and C. V. Shank, *Science*, 1991, **254**, 412–415.
16 A. S. Chatterley, C. W. West, M. G. Roberts and V. G. Verlet, *J. Phys. Chem. Lett.*, 2014, **5**, 843–848.
17 M. H. Farag, T. L. C. Jansen and J. Knoester, *Phys. Chem. Chem. Phys.*, 2018, **20**, 12746–12754.
18 J.-M. L. Pecourt, J. Peon and B. Kohler, *J. Am. Chem. Soc.*, 2001, **123**, 10370–10378.
19 A. J. Musser, C. Schnedermann, T. Wende, T. B. Kehoe, A. Rao and P. Kukura, *Nat. Phys.*, 2015, **11**, 352–357.
20 J. S. Lim and S. K. Kim, *Nat. Chem.*, 2010, **2**, 627–632.
21 C. Curutchet and B. Mennucci, *Chem. Rev.*, 2017, **117**, 294–343.
22 M. V. Berry, *Proc. R. Soc. Lond. A*, 1984, **392**, 45–57.
23 C. A. Mead, *Rev. Mod. Phys.*, 1992, **64**, 51–85.
24 H. C. Longuet-Higgins, U. Opik, M. H. L. Pryce and R. A. Sack, *Proc. R. Soc. London, Ser. A*, 1958, **244**, 1.
25 I. G. Ryabinkin, L. J.-Doriol and A. F. Izmaylov, *Acc. Chem. Res.*, 2017, **50**, 1785–1793.
26 C. Xie, C. L. Malbon, H. Guo and D. R. Yarkony, *Acc. Chem. Res.*, 2019, **52**, 501–509.
27 S. C. Althorpe, *J. Chem. Phys.*, 2006, **124**, 084105.
28 W. Domcke and D. R. Yarkony, *Ann. Rev. Phys. Chem.*, 2012, **63**, 325–354.
29 N. Moiseyev, M. Šindelka and L. S. Cederbaum, *J. Phys. B: At. Mol. Opt. Phys.*, 2008, **41**, 221001.

30 M. Pawlak, T. Szidarovszky, G. J. Halász and A. Vibók, *Phys. Chem. Chem. Phys.*, 2020, **22**, 3715–3723.

31 G. J. Halász, M. Šindelka, N. Moiseyev, L. S. Cederbaum and A. Vibók, *J. Phys. Chem. A*, 2012, **116**, 2636–2643.

32 G. J. Halász, A. Vibók and L. S. Cederbaum, *J. Phys. Chem. Lett.*, 2015, **6**, 348.

33 P. Badankó, G. J. Halász, L. S. Cederbaum, A. Vibók and A. Csehi, *J. Chem. Phys.*, 2018, **149**, 181101.

34 P. V. Demekhin and L. S. Cederbaum, *J. Chem. Phys.*, 2013, **139**, 154314.

35 G. J. Halász, A. Vibók, N. Moiseyev and L. S. Cederbaum, *J. Phys. B: At. Mol. Opt. Phys.*, 2012, **45**, 135101.

36 A. Csehi, G. J. Halász, L. S. Cederbaum and A. Vibók, *Faraday Discuss.*, 2016, **194**, 479.

37 C.-C. Shu, K.-J. Yuan, D. Dong, I. R. Petersen and A. D. Bandrauk, *J. Phys. Chem. Lett.*, 2017, **8**, 1–6.

38 G. J. Halász, L. S. Cederbaum and A. Vibók, *J. Phys. Chem. Lett.*, 2017, **8**, 1624–1630.

39 A. Tóth, A. Csehi, G. J. Haláz and A. Vibók, *Phys. Rev. A*, 2019, **99**, 043424.

40 T. Szidarovszky, G. J. Halász, A. G. Császár and A. Vibók, *J. Phys. Chem. Lett.*, 2018, **9**, 2739–2745.

41 F. Bouakline, *Chem. Phys.*, 2014, **442**, 31–40.

42 F. Bouakline, *J. Phys. Chem. Lett.*, 2018, **9**, 2271–2277.

43 G. J. Halász, A. Vibók, M. Šindelka, N. Moiseyev and L. S. Cederbaum, *J. Phys. B: At. Mol. Opt. Phys.*, 2011, **44**, 175102.

44 J. A. Hutchison, T. Schwartz, C. Genet, E. Devaux and T. W. Ebbesen, *Angew. Chem. Int. Ed.*, 2012, **51**, 1592–1596.

45 T. W. Ebbesen, *Acc. Chem. Res.*, 2016, **49**, 2403–2412.

46 M. Kowalewski and S. Mukamel, *Proc. Natl. Acad. Sci. U.S.A.*, 2017, **114**, 3278–3280.

47 A. Thomas, L. Lethuillier-Karl, K. Nagarajan, R. M. A. Vergauwe, J. George, T. Chervy, A. Shalabney, E. Devaux, C. Genet, J. Moran and T. W. Ebbesen, *Science*, 2019, **363**, 615–619.

48 T. Szidarovszky, G. J. Halász, A. G. Császár and A. Vibók, *J. Phys. Chem. Lett.*, 2018, **9**, 6215–6223.

49 A. Csehi, M. Kowalewski, G. J. Haláz and A. Vibók, *New J. Phys.*, 2019, **21**, 093040.

50 J. F. Triana, D. Peláez and J. L. Sanz-Vicario, *J. Phys. Chem. A*, 2018, **122**, 2266–2278.

51 M. Kowalewski, K. Bennett and S. Mukamel, *J. Phys. Chem. Lett.*, 2016, **7**, 2050–2054.

52 J. F. Triana and J. L. Sanz-Vicario, *Phys. Rev. Lett.*, 2019, **122**, 063603.

53 V. Rokaj, D. M. Welakuh, M. Ruggenthaler and A. Rubio, *J. Phys. B: At. Mol. Opt. Phys.*, 2018, **51**, 034005.

54 C. Schäfer, M. Ruggenthaler and A. Rubio, *Phys. Rev. A*, 2018, **98**, 043801.

55 O. Vendrell, *Chem. Phys.*, 2018, **509**, 55–65.

56 A. Semenov and A. Nitzan, *J. Chem. Phys.*, 2019, **150**, 174122.

57 A. Mandal, T. D. Krauss and P. Huo, *J. Phys. Chem. B*, 2020, **124**, 6321–6340.

58 E. A. Power and S. Zienau, *Philos. Trans. R. Soc. London, Ser. A*, 1959, **251**, 427–454.

59 C. Cohen-Tannoudji, J. Dupont-Roc and G. Grynberg, *John Wiley & Sons, Inc.: Hoboken, U.S.A.*, 1989.

60 C. Schäfer, M. Ruggenthaler and A. Rubio, *Phys. Rev. A*, 2018, **98**, 043801.

61 O. Vendrell, *Chem. Phys.*, 2018, **509**, 55–65.

62 A. Mandal, S. Montillo and P. Huo, *J. Phys. Chem. Lett.*, 2020, **11**, 9215–9223.

63 T. J. Giese and D. M. York, *J. Chem. Phys.*, 2004, **120**, 7939–7948.

64 M. H. Beck, A. Jäckle, G. Worth and H.-D. Meyer, *Physics Reports*, 2000, **324**, 1–105.

65 R. S. Mulliken, *J. Am. Chem. Soc.*, 1952, **74**, 811–824.

66 R. J. Cave and M. D. Newton, *Chem. Phys. Lett.*, 1996, **249**, 15 – 19.

67 R. J. Cave and M. D. Newton, *J. Chem. Phys.*, 1997, **106**, 9213–9226.

68 N. S. Hush, *John Wiley & Sons, Inc.: Hoboken, U.S.A.*, 2007.

69 C. Wittig, *Phys. Chem. Chem. Phys.*, 2012, **14**, 6409–6432.

70 C. Xie, B. K. Kendrick, D. R. Yarkony and H. Guo, *J. Chem. Theory Comput.*, 2017, **13**, 1902–1910.

71 C. Xie, D. R. Yarkony and H. Guo, *Phys. Rev. A*, 2017, **95**, 022104.

72 M. Kowalewski, K. Bennett and S. Mukamel, *J. Chem. Phys.*, 2016, **144**, 054309.

73 J. W. Zwanziger, M. Koenig and A. Pines, *Annu. Rev. Phys. Chem.*, 1990, **41**, 601–646.

74 A. F. Izmaylov, J. Li and L. J.-Doriol, *J. Chem. Theory Comput.*, 2016, **12**, 5278–583.

75 G. J. Halász, P. Badankó and A. Vibók, *Mol. Phys.*, 2018, **116**, 2652–2659.

76 V. Rokaj, D. M. Welakuh, M. Ruggenthaler and A. Rubio, *J. Phys. B: At. Mol. Opt. Phys.*, 2018, **51**, 034005.

77 C. Schäfer, M. Ruggenthaler, V. Rokaj and A. Rubio, *ACS Photonics*, 2020, **7**, 975–990.

78 S. C. Althorpe, T. Stecher and F. Bouakline, *J. Chem. Phys.*, 2008, **129**, 214117.

79 A. Natan, M. R. Ware, V. S. Prabhudesai, U. Lev, B. D. Bruner, O. Heber and P. H. Bucksbaum, *Phys. Rev. Lett.*, 2016, **116**, 143004.

80 L. J.-Doriol, I. G. Ryabinkin and A. F. Izmaylov, *J. Chem. Phys.*, 2013, **139**, 234103.